CrystEngComm

ROYAL SOCIETY
OF CHEMISTRY

PAPER
Patrick M. J. Szell, Józef R. Lewandowski, Helen Blade,
Leslie P. Hughes, Sten O. Nilsson Lill and Steven P. Brown
Taming the dynamics in a pharmaceutical by cocrystallization:
investigating the impact of the coformer by solid-state NMR

Check for updates

Taming the dynamics in a pharmaceutical by cocrystallization: investigating the impact of the coformer by solid-state NMR†

Patrick M. J. Szell, [iD] [a] Józef R. Lewandowski, [iD] [b] Helen Blade, [iD] [c] Leslie P. Hughes, [iD] *[c] Sten O. Nilsson Lill [iD] [d] and Steven P. Brown [iD] *[a]

Pharmaceuticals in their crystalline state may display a range of dynamics that can affect their physicochemical properties and chemical stability. With pharmaceutical cocrystals continuing to gain attention, there is an opportunity to investigate how the dynamics are changing in these new solid forms. Here, we investigate the dynamics in efavirenz, an anti-HIV drug, and a series of its cocrystals using a combination of DFT calculations and solid-state magic-angle spinning (MAS) NMR spectroscopy. We show that the crystalline form of efavirenz has a highly dynamic cyclopropyl group, and displays additional rocking motion. In contrast, the dynamics in the efavirenz cocrystals appear to be tamed, with the cyclopropyl group in the (efavirenz)(L-proline) cocrystal being the most constrained, and these constraints originating from a more favourable crystal packing in the cocrystals.

Pharmaceutical cocrystallization is a recent strategy where an active pharmaceutical ingredient (API) is crystallized with one or more coformers.[1–3] This approach can provide control of the physicochemical properties, having been shown to be highly beneficial, for example, in improving dissolution rates and mechanical properties.[4–7] Interestingly, cocrystals have also been shown to influence the chemical stability of an API,[8,9] potentially extending their shelf-lives. In recent years, the field of pharmaceutical cocrystals has flourished, with several commercial products now being available or under development.[10]

Despite the general conception that solids are rigid and fixed in place, molecules in their crystalline state may display a range of motions. In the context of this study, we refer to these motions as dynamics. Dynamics have been shown to be important for the function of proteins,[11–13] materials,[14] and molecular machines,[15,16] and can be modified by

[a] *Department of Physics, University of Warwick, Coventry, CV4 7AL, UK.*
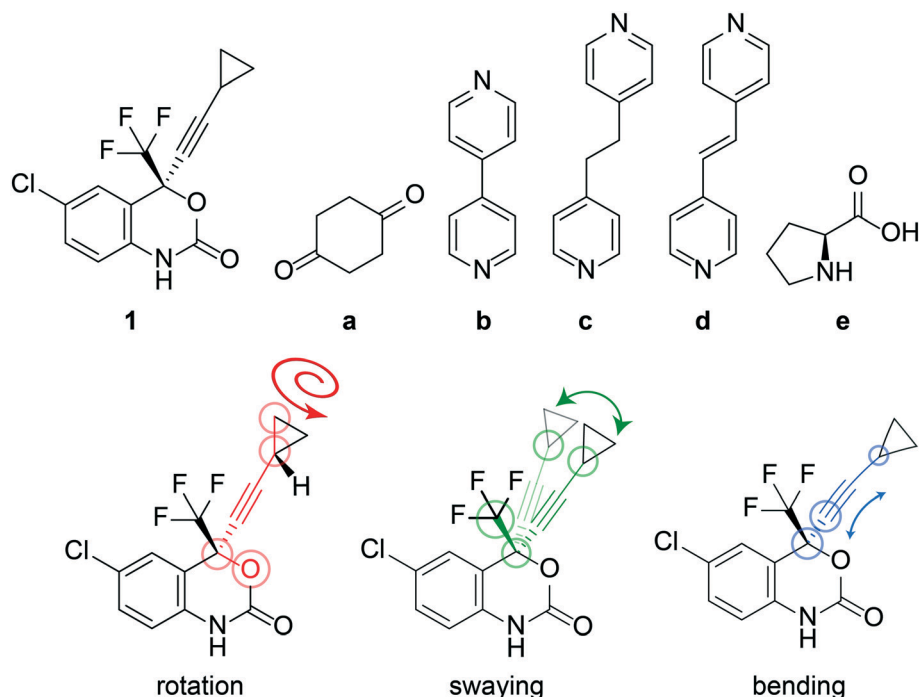*E-mail: S.P.Brown@warwick.ac.uk*
[b] *Department of Chemistry, University of Warwick, Coventry, CV4 7AL, UK*
[c] *Oral Product Development, Pharmaceutical Technology & Development,*
Operations, AstraZeneca, Macclesfield, UK. E-mail: Les.Hughes2@astrazeneca.com
[d] *Early Product Development and Manufacturing, Pharmaceutical Sciences, R&D,*
AstraZeneca, Gothenburg, Sweden

intermolecular interactions and the crystal packing.[17,18] However, molecular motion may be undesirable in pharmaceuticals as this has been shown to influence their chemical and physical stabilities.[19–21] In addition, dynamics can render an API difficult to crystallize, making the development of a commercially relevant process challenging, while also complicating the process of structural characterization due to the added uncertainty inherent with crystallographic disorder.[22] As a result, the ability to control dynamics may lead to better quality drug products with a consistent performance and improved manufacturability. Recent work has shown that dynamics in crystalline solids can be influenced by manipulating the chemical environment,[23,24] the crystallographic environment,[22,25,26] or by introducing a dynamics catalyst.[27] More specifically, the dynamics present in crystalline pharmaceuticals have previously been investigated,[28–31] showing an impact on the dynamics for preparing new polymorphs,[32] the salt form,[33,34] or even pharmaceuticals supported in a matrix.[35,36] However, to the best of our knowledge, there is no systematic investigation on how the dynamics change in pharmaceuticals as coformers are introduced into the structure. With the rise of pharmaceutical cocrystals, insights on how the dynamics are being modified in these new solid forms can provide crucial structural understandings on the next generation of medicines.

The anti-HIV pharmaceutical efavirenz (**1**) features a dynamic cyclopropyl group that adopts multiple crystallographic positions,[37] and a trifluoromethyl group which is known to rotate (see Fig. 1). Having a dynamic

Fig. 1 (Top) Diagram of the molecular structures used in this study: (**1**) efavirenz, (**a**) cyclohexane-1,4-dione, (**b**) 4,4′-bipyridine, (**c**) 1,2-di(pyridin-4-yl) ethane, (**d**) (*E*)-1,2-di(pyridin-4-yl)ethene and (**e**) L-proline. (Bottom) Molecular structure of **1** illustrating the rotation of the cyclopropyl group associated with a change in the O–C–C–C torsion angle, $\theta_{\text{O–C–C–C}}$ (red circled atoms), the swaying of the cyclopropyl group associated with a change in the C–C–C angle, θ_{sway} (green circled atoms), and the bending of the ethynyl–cyclopropyl axis, θ_{bend} (blue circled atoms).

moiety and several of its cocrystals reported in the Cambridge Structural Database (CSD),[37–40] **1** provides an ideal opportunity to investigate if the dynamics are changing in the cocrystals. Here, we investigate the dynamics of the cyclopropyl group in **1** and a series of its reported cocrystals,[37–39] as shown in Fig. 1, using a combination of DFT calculations and solid-state NMR. Several polymorphs of **1** have previously been reported, however only form I is investigated here as it is the most stable of the polymorphs.[37]

In this work, information on the dynamics of **1** is obtained using ^{13}C cross polarisation (CP) and ^{19}F solid-state magic-angle spinning (MAS) NMR spectroscopy under the theme of NMR crystallography.[41,42] Spin–lattice (T_1) relaxation time measurements are applied to extract the thermodynamic parameters of the fast ps-ns motion of the cyclopropyl ring, and is interpreted using the Bloembergen–Purcell–Pound (BPP) relaxation theory.[43,44] These data are summarized in terms of their correlation times (τ), which characterise the average rate of the dynamic events, and the activation energy (E_a), the average energy of a dynamic process occurring on the NMR timescale. The activation energies were further investigated using transition state (TS) calculations, potential energy surface calculations, and an analysis of the interaction energies in each crystal structure. Overall, the objective of this work is to investigate the dynamics present in **1** and whether cocrystallization may be a viable strategy to reduce undesired dynamics in a pharmaceutical.

Results

i) X-ray diffraction

The crystal structure of **1**, reported by Mahapatra *et al.*,[37] features three molecules in the asymmetric unit ($Z' = 3$), with one of the cyclopropyl groups exhibiting crystallographic disorder over two positions. The nature of the disordered cyclopropyl group in **1** appears to be dynamic in origin, and consists of a rotation of 136 ± 35° along the ethynyl axis, with the error considering the sizes of the atomic displacement parameters (ADPs) as represented by thermal ellipsoids and shown in Fig. 2. This corresponds to a rotation whereby the torsion angle between the cyclopropyl group axis and the efavirenz axis ($\theta_{\text{O–C–C–C}}$, see Fig. 1) range from −42 ± 26° to 94 ± 24° (see Table S37†). Further, as illustrated in Fig. 1, the experimental structure reveals a swaying of the entire cyclopropylethynyl group and a bending of the C–C≡C–C axis from linearity, corresponding to a change in θ_{sway} and θ_{bend} of 17 ± 15° and 29 ± 30°, respectively (see Tables S38 and S39†). In addition, there is a rocking motion of the double ring backbone, which is manifested in the crystal structure as an elongation of the thermal ellipsoids for most non-cyclopropyl atoms in **1**, as shown in Fig. 2. These dynamics are investigated further in the cocrystals.

The crystal structures of cocrystals **1a** and **1d**, reported by Mahapatra *et al.*[37] and de Melo *et al.*,[38] respectively, do not have crystallographic disorder but the ADPs of the cyclopropyl group are distorted. The crystal structures of
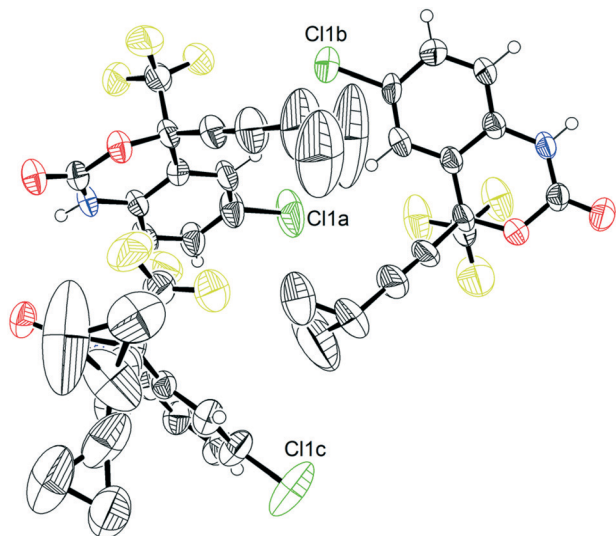
Fig. 2 Thermal ellipsoid plot of pure **1**.[45] This figure was generated for the X-ray diffraction structure CSD# 767883 from Mahapatra et al.[37]

cocrystals **1b** and **1c**, reported by Mahapatra et al.[37] and de Melo et al.,[38] respectively, both have dynamic crystallographic disorder and some distortions in the ADPs of the cyclopropyl groups. Structure **1e** is a cocrystal featuring the zwitterion form of L-proline, and was reported by Marques et al.[39] Structure **1e** is not disordered and has been solved from powder diffraction using isotropic displacement parameters and constraints on bond lengths and angles. All other structures apart from **1e** have been solved by single crystal X-ray diffraction, and their ORTEP plots[45] can be found in Fig. S37–S41 of the ESI.† The thermal ellipsoids of all atoms in the structure, which are a measure of the uncertainty on the atomic positions arising from the magnitude and direction of the thermal vibrations of atoms, are significantly larger for **1** than in the cocrystals. The average volume of the

thermal ellipsoids of the CH_2 carbon atoms of the cyclopropyl groups were calculated at a 50% ellipsoid probability and, as shown in Table 1, is largest in **1** and decreases in the cocrystals, suggesting the occurrence of reduced dynamics of the cyclopropyl group in the cocrystals. While there are additional cocrystals with **1** reported in the literature,[46,47] we have restricted our investigations to the structures available in the CSD.[40] Selected experimental X-ray parameters have been summarized in Table 2.

ii) DFT calculations

In this section, different types of DFT calculations are applied to probe and rationalise the observed dynamics. First, DFT calculations featuring the periodicity of the crystal lattice were performed to investigate the origins of the energy barriers of the cyclopropyl dynamics using CASTEP transition state calculations. All structures were initially optimized using CASTEP, giving rise to small differences in $\theta_{O–C–C–C}$, θ_{sway} and θ_{bend} (see Tables S37–S39 of the ESI†). As structures **1a**, **1d**, and **1e** did not have disordered cyclopropyl groups, the transition state calculations were limited to structures **1**, **1b**, and **1c**, and were performed by specifying the disordered positions as the starting and end points to the calculations. In the case of **1**, the calculated motion of the cyclopropyl group was a $\Delta\theta_{O–C–C–C} = 121.2°$ rotation around the ethynyl axis, a swaying of the cyclopropyl group ($\Delta\theta_{sway} = 4.8°$), a bending of the ethynyl group ($\Delta\theta_{bend} = 10.3°$), and a rocking motion of the double ring backbone, as shown in Fig. 3, with a calculated energy barrier of 8.8 kJ mol^{-1}. The calculated motion in **1b** and **1c** were rotations of $\Delta\theta_{O–C–C–C} = 60.5°$ and 79.5° for the cyclopropyl group along the ethynyl axis, respectively, a small bending of the ethynyl group ($\Delta\theta_{bend}$ of 12.5° for **1b**, 10.4° for **1c**), some swaying ($\Delta\theta_{sway} = 2.9°$ for **1b**, 7.9° for **1c**), and a slight amount of rocking motion (see Fig.

Table 1 Selected X-ray crystallography parameters, DFT-calculated energy of all through-space interactions involving the selected cyclopropyl group, and activation energy & correlation times derived from the $T_1(^{13}C)$ NMR relaxation experiments for the cyclopropyl groups in **1** and cocrystals **1a–1e**

Sample	X-ray Thermal ellipsoids volume^a (Å^3)	DFT Interaction energy^b (kJ mol^{-1})	^{13}C NMR relaxation $E_a^{~c}$ (kJ mol^{-1})	$\tau_{25°C}$/s	Assignment^d
1	2.72	−95.3	12 ± 2 [8.8]	$(3.1 ± 1.0) × 10^{-11}$	Site 1^{f,g}
		−142.3	10 ± 2	$(1.3 ± 0.5) × 10^{-11}$	Site 2^g
		−99.4	11 ± 2	$(1.1 ± 0.3) × 10^{-12}$	Site 3^g
1a	1.80	−163.9	8 ± 2	$(2.6 ± 0.9) × 10^{-12}$	Site 1
		−120.4			Site 2
1b	1.09	−149.2	2 ± 1 [2.1]	$(5.6 ± 1.1) × 10^{-13}$	Site 1^f
		−142.5			Site 2^f
1c	0.58	−145.8	4 ± 2 [5.3]	$(1.0 ± 0.4) × 10^{-12}$	Site 1
		−142.5			Site 2^f
1d	0.40	−149.2	3 ± 1	$(6.4 ± 1.0) × 10^{-13}$	Site 1
		−150.6			Site 2
1e	0.25^e	−218.3	1 ± 1	$(1 ± 2) × 10^{-13}$	Site 1

^{a} Average volume of the thermal ellipsoids (calculated at a 50% ellipsoid probability) of the CH_2 carbon atoms on the cyclopropyl group. ^{b} Breakdown given in Tables S13–S24.† ^{c} DFT-calculated E_a are given in brackets. ^{d} Crystallographic assignments are given in Table S37 of the ESI.† ^{e} Isotropic thermal ellipsoids. ^{f} Site is crystallographically disordered. ^{g} Obtained from three resolved features at $\delta(^{13}C)$: 8.8 ppm, 8.0 ppm, and 7.4 ppm, respectively.

Table 2 Selected experimental X-ray crystallography parameters of the samples investigated in this work

Sample	Acquisition temperature (K)	R-Factor (%)	Thermal ellipsoids volume[a] (Å^3)	Diffraction technique	CSD # (REFCODE)	Ref.
1	250	6.56	2.72	Crystal	767883 (AJEYAQ02)	Mahapatra et al.[37]
1a	293	9.43	1.80	Crystal	768815 (QUSREC)	Mahapatra et al.[37]
1b	298	4.73	1.09	Crystal	767759 (QUSQOL)	Mahapatra et al.[37]
1c	120	3.79	0.58	Crystal	909386 (XICRUY)	de Melo et al.[38]
1d	120	7.80	0.40	Crystal	909385 (XICSAF)	de Melo et al.[38]
1e	298	3.59	0.25[b]	Powder	1847168 (HUDRAC)	Marques et al.[39]

[a] Volume of the anisotropic displacement parameter (ADP) of the CH_2 group of the cyclopropyl group on the efavirenz molecule at a 50% probability. The volume was calculated using the equation: $\text{volume} = \frac{4}{3}\pi(U_{11} \cdot U_{22} \cdot U_{33})$ using U_{ij} converted to units of Å. [b] Isotropic thermal ellipsoids.
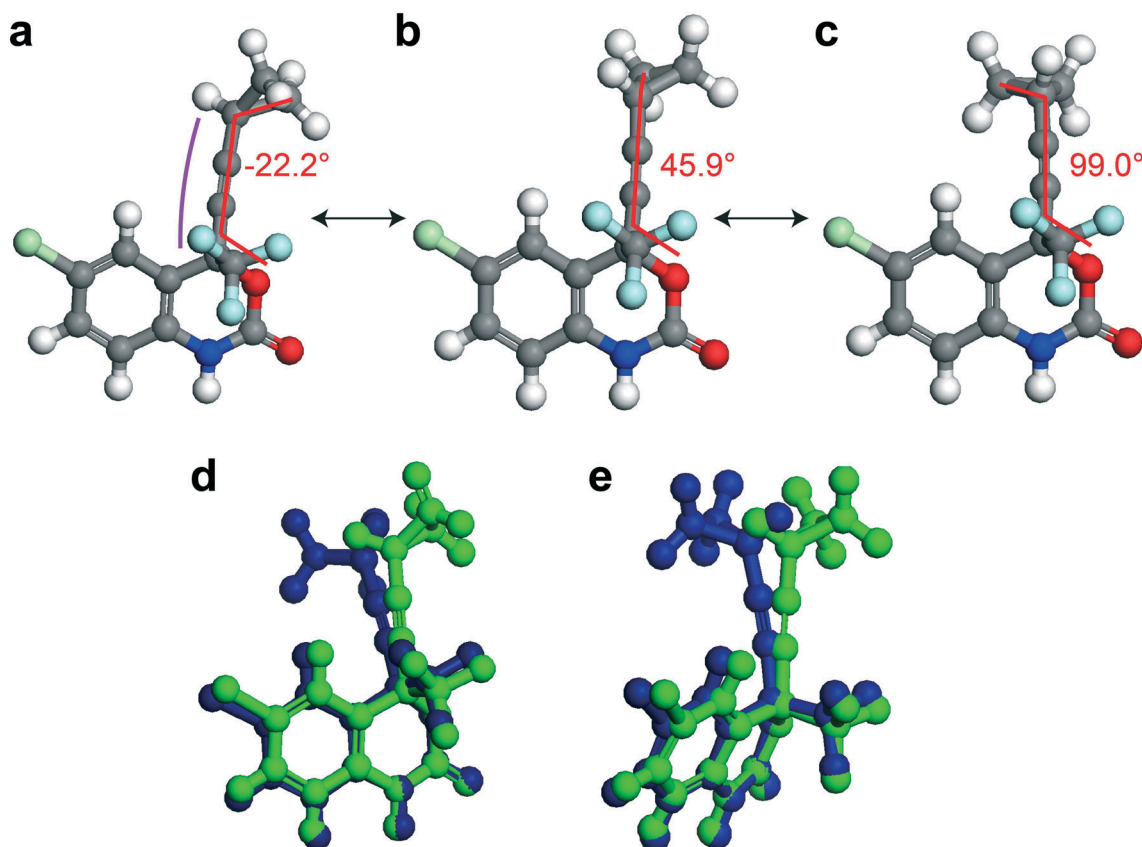
Fig. 3 (a) Starting position (C16A C17A C18A), (b) transition state, and (c) ending position (C16B C17B C18B) of the disordered cyclopropyl group in **1** as determined from CASTEP transition state calculations. The red line denotes the torsion angle ($\theta_{O-C-C-C}$), and the magenta line highlights the bending angle (θ_{bend}). (d and e) Overlay of the starting position (green) and ending position (blue) from two viewing angles. Only the disordered molecule in **1** is shown for clarity.

S33 and S34 of the ESI†). The calculated energy barriers for **1b** and **1c** were 2.1 kJ mol^{-1} and 5.3 kJ mol^{-1}.

Potential energy surfaces (PES) were calculated with DMol3 using DFT for the rotation of the cyclopropyl group of the efavirenz molecule, corresponding to systematically changing the $\theta_{O-C-C-C}$ torsion angle, and are in close agreement with the TS results obtained from CASTEP. In all cases, the calculations were performed using a periodic model of their respective crystal structure. Intriguingly, as shown in Fig. 4, the PES calculations reveal a broad energy well with two minima in **1**, **1b**, and **1c**, supporting the

dynamic crystallographic disorder observed in their X-ray structures. The barriers are small in samples **1**, **1b**, and **1c**, and appear to be higher in **1**. In the case of **1d**, while there is only one position of the cyclopropyl group in the X-ray structure, the DFT-calculated energy well is also broad but in this case there is a single energy minimum with an elevated rotational energy barrier. The PES for both cyclopropyl sites in **1b**, **1c**, and **1d** were similar. In contrast, the energy profiles of **1a** and **1e** are narrower with higher barriers resulting in crystal structures constrained in a single cyclopropyl orientation. As there are two unique cyclopropyl groups in
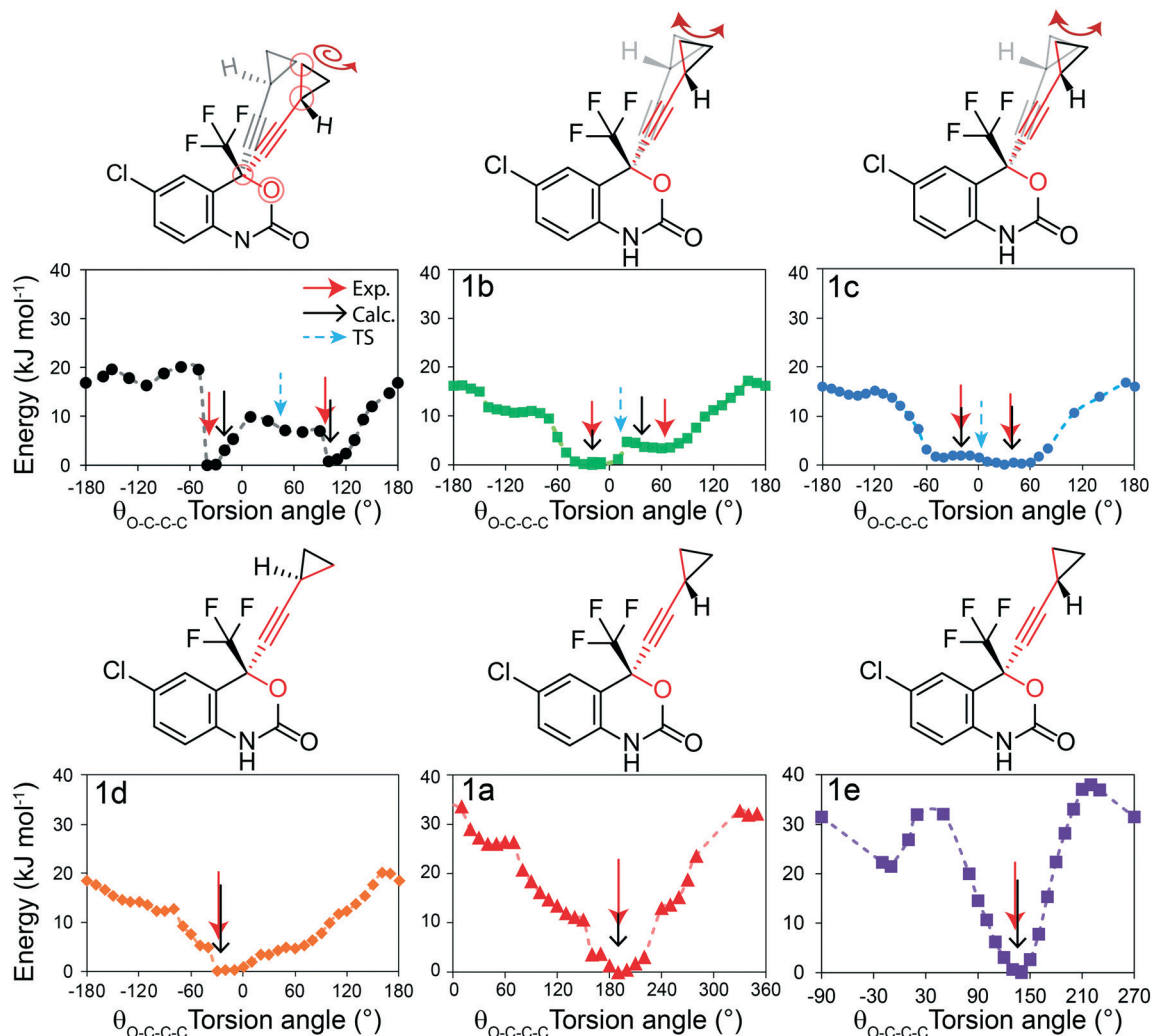
Fig. 4 DFT-calculated potential energy surface for the rotation of a cyclopropyl group along the ethynyl axis in **1** (site 1), **1b** (site 2), **1c** (site 2), **1d** (site 2), **1a** (site 1), and **1e** (site 1). The molecular structures above highlight the $\theta_{O-C-C-C}$ torsion angle and the cyclopropyl orientations. The *Y*-axis reports the relative energy. The torsion angles from the X-ray structure (exp.), DFT-optimized structure (calc.), and DFT-calculated transition state are indicated by the red, black, and blue arrows, respectively, and are tabulated in Table S37 of the ESI.†

the crystal structure of **1a** ($Z' = 2$), the PES has been computed for both groups. Cyclopropyl site 1 for **1a** has a calculated energy barrier of 33 kJ mol^{-1} (see Fig. 4), whereas cyclopropyl site 2 for **1a** has a calculated energy barrier of 14 kJ mol^{-1} (see Fig. S36 of the ESI†). In **1e**, additional constraints on the cyclopropyl ring results in a narrow energy well with a barrier of 32 kJ mol^{-1} and 38 kJ mol^{-1} on the sides of the minimum. Consequently, a single preferred cyclopropyl position is observed in **1e**, in agreement with the X-ray crystal structure.

In order to provide greater context for the impact of the crystallographic environment on the energy barrier, the calculation was repeated on an isolated molecule of **1**, with the PES shown in Fig. S35 of the ESI.† The calculated rotational barrier for the cyclopropyl group in an isolated molecule was 2.6 kJ mol^{-1}, which is in excellent agreement with the 2.8 kJ mol^{-1} reported in a previous investigation.[37] In the investigation reported here, the higher energy barriers

observed computationally in **1**, **1a**–**1e** originate from constraints arising from through-space interactions involving neighbouring molecules in the crystal.

DFT calculations (with GAUSSIAN16) were used to estimate the total energy of the through-space interactions involving each cyclopropyl group, and is referred to here as the total interaction energy.[48,49] Sample **1** has the least constraining environment of all samples and the cocrystals have a higher number of constraining interactions, as shown in Fig. 5, summarized in Table 1, and fully tabulated in Tables S13–S24 of the ESI.† For instance, the disordered cyclopropyl group in **1** (site 1) features five interactions from neighbouring molecules, with the sum of the interaction energies being −95.3 kJ mol^{-1}. The sum of the interaction energies in the cocrystals are progressively higher at −120.4 kJ mol^{-1} in **1a** (site 2), and −149.2 kJ mol^{-1} in **1d** (site 1). In stark contrast, the cyclopropyl group in **1e** interacts primarily with four adjacent cyclopropyl groups from neighbouring
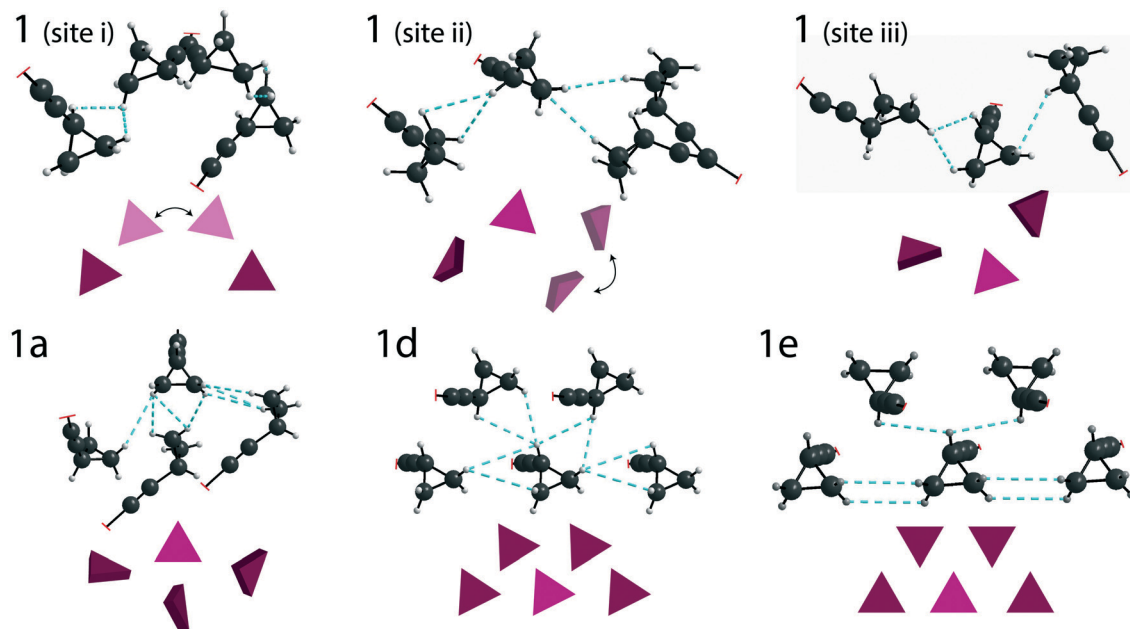
Fig. 5 Depiction of the crystallographic packing around the cyclopropyl group for the three distinct cyclopropyl groups in **1** (above) and one of the two cyclopropyl groups in **1a** (site 2), **1d** (site 1), and **1e** (site 1). The crystal packing of **1b**, **1c**, and **1d** are similar. A simplified depiction of the packing is shown, with the triangles representing the cyclopropyl group. The black arrows in **1** highlight the two positions of the disordered groups.

molecules, as shown in Fig. 5. The sum of all interactions involving the cyclopropyl group in **1e** (site 1), which also includes two weaker interactions, has a total interaction energy of −218.3 kJ mol⁻¹. Although **1e** has a zwitterion L-proline molecule in the structure, there are no interactions involving the cyclopropyl group and the L-proline molecule. Interestingly, the cyclopropyl groups in all cases interact with other molecules of **1** rather than the coformer.

iii) Solid-state NMR

Solid-state NMR experiments observing both the ^{13}C and ^{19}F nucleus were applied to confirm the structural models and to observe changes in the ^{13}C and ^{19}F chemical shifts ($\delta(^{13}$C), $\delta(^{19}$F)). There have been previous reports of ^{13}C solid-state NMR experiments to characterize **1**, and the results presented here are in good agreement.[50,51] As shown in Fig. 6i, the ^{13}C
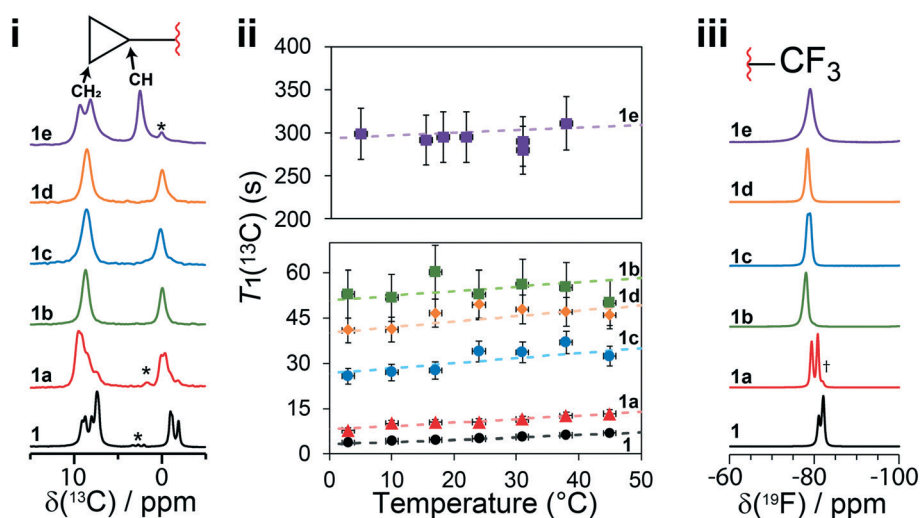

Fig. 6 (i) ^{13}C CPMAS solid-state NMR spectra of **1** and cocrystals **1a** to **1e**, with a magnified view of the cyclopropyl resonances. (ii) $T_1(^{13}$C) relaxation times of the CH_2 carbon atoms of the cyclopropyl ring at several temperatures. (iii) ^{19}F one-pulse solid-state MAS NMR spectra of the CF_3 group in **1** and cocrystals **1a** to **1e**. The dashed lines in (ii) denote the fits to eqn (S5),† and the Y-axis scale is different for the top (**1e**) and bottom (**1** and **1a** to **1d**) parts. The asterisks denote spinning sidebands, and the dagger denotes a trace amount of starting material ($\nu_L(^1$H) = 500 MHz, ν_{MAS} = 11 750 Hz). Errors on $T_1(^{13}$C) are estimated to be 10%.

solid-state NMR spectra show clear $\delta(^{13}C)$ changes between **1** and cocrystals **1a–1e** for the resonances assigned to the CH$_2$ and CH carbons of the cyclopropyl group. For instance, a $\delta(^{13}C)$ difference of 4.4 ppm is observed between structures **1** and **1e** for the CH carbon of the cyclopropyl group. The full ^{13}C NMR spectra are reported in Fig. S19–S24† together with assignments based on GIPAW DFT calculations and discussed further in the ESI.† The ^{19}F solid-state NMR spectra provide a secondary indicator for the successful preparation of the cocrystals, observing $\delta(^{19}F)$ changes of up to 3.6 ppm, for instance, between **1** and **1e**. A small amount (~5%, denoted by a dagger) of residual **1** has been identified from the ^{13}C, ^{19}F, and PXRD of **1a**. Fortunately, the chemical shifts in **1a** were sufficiently resolved from the starting material not to affect the T_1 measurements.

The $T_1(^{13}C)$ relaxation times provide direct insights into the dynamics occurring on the ps–ns timescales and have been measured at several temperatures from 3 °C to 45 °C. Upon the occurrence of motion with a given amplitude near the ^{13}C Larmor frequency (ω_L = 125.9 MHz in this case), the $T_1(^{13}C)$ relaxation times are shorter (<30 s), such as in **1** and **1a**, and are shortest when the rate of the dynamics (τ^{-1}) is at the Larmor frequency ($\tau \approx 1/\nu_L$). In this work, the longer $T_1(^{13}C)$ relaxation times (>30 s), such as for **1b**, **1c**, **1d** and **1e**, are associated with dynamics occurring at a rate faster than the ^{13}C Larmor frequency ($\tau \ll 1/\omega_L$). Being the inverse of the rate, we assume the correlation time at a given temperature ($\tau_{x°C}$) follows the Arrhenius equation (see eqn (S2)†) and can be calculated from the preexponential factor, τ_0, and the activation energy, E_a. The E_a is an Arrhenius parameter that describes the average energy of a dynamic process occurring in this timescale. Both E_a and τ_0 are used to calculate (see eqn (S3)†) the spectral density function, $J(\omega_L,\tau)$, which is used to calculate $T_1(^{13}C)$. As a result, fitting the $T_1(^{13}C)$ relaxation time at several temperatures allows for both τ_0 and E_a to be determined. For protonated carbons, including the CH$_2$ and CH carbon atoms of the cyclopropyl group, the ^{13}C–^1H dipolar coupling relaxation mechanism

dominates the $T_1(^{13}C)$. Moreover, because samples contain ^{13}C at natural abundance, averaging of the rates due to proton driven spin diffusion typically observed in the solid state for ^{13}C labelled systems is not a concern.[52]

In the case of **1**, the $T_1(^{13}C)$ relaxation times of the CH$_2$ atoms of the cyclopropyl group are the shortest of all samples investigated here, ranging between 0.2 s to 2.0 s. Furthermore, as shown in Fig. 7, the short $T_1(^{13}C)$ relaxation times extend to carbon atoms well beyond the cyclopropyl group, with the ethynyl carbons and even all other protonated carbon atoms on **1** having $T_1(^{13}C)$ values of less than 15 seconds, and are orders of magnitude shorter than in the cocrystals. Additional $T_1(^{13}C)$ plots for the other resonances of **1** are shown in Fig. S31 and S32 of the ESI.† The $T_1(^{13}C)$ relaxation times of the CH$_2$ cyclopropyl atoms in **1a** are slightly longer than for **1**, with values of up to 12.7 seconds. As shown in Fig. 6ii, the $T_1(^{13}C)$ relaxation times of the CH$_2$ carbons are much longer in cocrystals **1b**, **1c**, and **1d**, with $T_1(^{13}C)$ values of up to 60 seconds. In stark contrast, the $T_1(^{13}C)$ relaxation times of **1e** are on the order of 300 seconds, supporting the occurrence of significant changes to the dynamics.

For each sample, the $T_1(^{13}C)$ relaxation times of the CH$_2$ carbon atoms of the cyclopropyl group have been fitted using eqn (S5) from the ESI† assuming the presence of a single dominant motional mode, with the resulting fits shown on Fig. 6ii. The fitting parameters have been tabulated in Table 1, summarizing the activation energy (E_a) and the correlation time at 25 °C ($\tau_{25°C}$). These parameters were verified by fitting the $T_1(^{13}C)$ relaxation times of the CH carbon atom of the cyclopropyl group, with all parameters being in excellent agreement. Using the NMR assignments obtained from the GIPAW calculations, the thermodynamic parameters have been assigned to their crystallographic site. The activation energy is highest in **1** at 12 ± 2 kJ mol^{-1} and is in close agreement with the CASTEP transition state calculations. The slightly lower energy barrier (8.8 kJ mol^{-1}) obtained from these calculations were likely due to being performed on a reduced model of **1** as

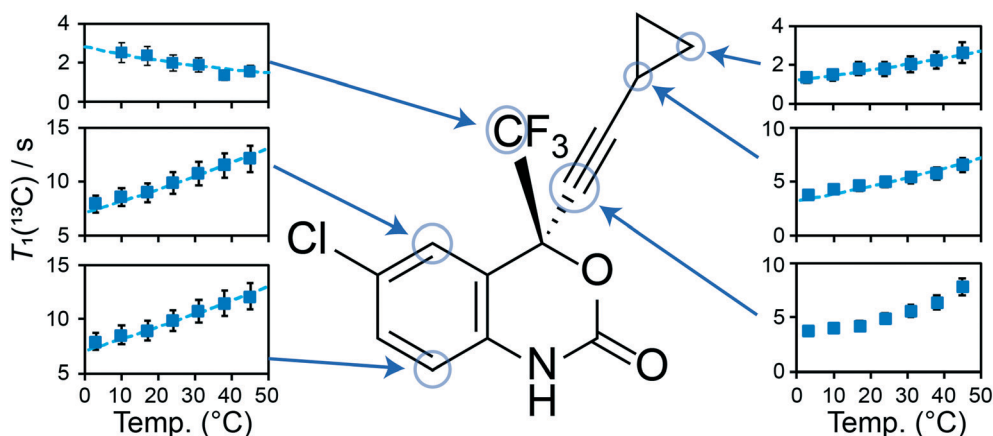**Fig. 7** $T_1(^{13}C)$ for selected carbon atoms in pure **1** as a function of the temperature. The dashed lines in the plots denote the fits for protonated carbons using eqn (S5)† (see Fig. 6ii and S31 and S32†). The $T_1(^{13}C)$ of the cyclopropylethynyl group were measured from the resonances assigned to the disordered molecule of **1**. The fitting parameters can be found in Table S10 of the ESI.†

a result of computational limitations. The dynamics in **1** are assigned to the total motion of the cyclopropyl group observed from the X-ray crystal structure and DFT calculations, that is, the rotation of the cyclopropyl group, the swaying of the cyclopropylethynyl moiety, and the bending of the ethynyl axis (see Fig. 1). The environment surrounding the disordered cyclopropyl ring in **1** appears to be loosely packed in the crystal structure (see Fig. 5), thus providing the required space for the group to rotate and sway. As shown in Fig. 7 and S31 and S32 of the ESI,† the $T_1(^{13}C)$ for the other protonated carbon atoms in **1** appear to follow the same thermal activation parameters as the cyclopropyl group, supporting the occurrence of a rocking motion of the double ring backbone. The E_a's are progressively lower in the cocrystals, with **1a** having an E_a of 8 ± 2 kJ mol^{-1} & **1e** having an E_a of 1 ± 1 kJ mol^{-1}, and **1b** and **1c** are in excellent agreement with the computational results. The low E_a measured in **1e** suggests that due to the heightened rotational energy barrier originating from the crystal packing, the cyclopropyl group does not rotate on the time scales to which T_1 measurements are sensitive to, with the experiment instead capturing local librations of the CH bonds in the cyclopropyl group. Interestingly, the two CH_2 carbons of the cyclopropyl group in **1e** are resolved in the ^{13}C NMR spectrum, further supporting the absence of chemical exchange by rotational motion at this timescale. With a decrease in E_a observed in the cocrystals, the $\tau_{25°C}$ of the dynamics in the cocrystals decreases, and $T_1(^{13}C)$ increases significantly.

Discussion

The experimental X-ray crystal structure shows that the cyclopropyl groups are highly dynamic in pure **1**, which is reflected by the occurrence of crystallographic disorder and distorted ADPs. Based on the crystal structure of **1**, the dynamics of the disordered cyclopropyl group have been assigned to a rotation along the ethynyl axis, a swaying of the entire cyclopropylethynyl group, a bending of the C–C≡C–C axis, and a rocking motion of the double ring backbone. The dynamics observed in the experimental crystal structure are also supported by DFT, calculating an energy barrier of 8.8 kJ mol^{-1} and reproducing the rocking motion. The DFT-calculated potential energy surface of **1**, as shown in Fig. 4, shows a relatively low energy barrier between the two experimentally observed crystallographic positions of the disordered cyclopropyl group, allowing for the rotation of the cyclopropyl group to occur. The experimental $T_1(^{13}C)$ relaxation data supports these observations, with a measured E_a of 12 ± 2 kJ mol^{-1} being in close agreement with the calculations. The short $T_1(^{13}C)$ across the entire molecule of **1**, as shown in Fig. 7, supports the occurrence of rocking motion, and appears to correlate with the dynamics of the cyclopropyl groups.

In contrast to **1**, there is a remarkable change in the dynamics occurring in the cocrystals. Given the reduction of these dynamics, we denote this effect as a taming of the dynamics. While there was no crystallographic disorder observed in the X-ray structures of **1a**, **1d**, and **1e**, dynamic crystallographic disorder with two separated cyclopropyl positions was observed in the structures of **1b** and **1c**. The DFT calculations ascribe the motion in **1b** and **1c** to a 61° and 79° rotation of the cyclopropyl group along the ethynyl axis, respectively, with a smaller amount of rocking motion. Moreover, the average volumes of the ADPs of the cyclopropyl's CH_2 atoms are significantly smaller in the cocrystals than in **1**, further supporting the occurrence of tamed dynamics. In **1b** and **1c**, the PES calculations suggests the occurrence of a broad double well energy minimum and low rotational energy barriers, with the cyclopropyl groups rotating between two positions within this minimum. In **1d**, while the energy minimum is also broad, there is only a single energy minimum. A significantly higher energy barrier is observed in **1e**, reflecting the presence of additional interactions constraining the cyclopropyl group.

The taming of the dynamics in **1** is in direct contrast to a previous investigation showing the potential of catalysing or promoting dynamics through the introduction of a halogenated coformer,[27,53,54] and can be rationalized by the crystal packing. As shown in Fig. 5, the crystallographic environment surrounding the disordered cyclopropyl group in **1** appears to be loosely packed, allowing the dynamics to occur with a total calculated interaction energy of −95.3 kJ mol^{-1}. Of all the samples investigated here, **1e** has the most tightly packed crystallographic environment, as shown in Fig. 5, and has a total calculated interaction energy of −218.3 kJ mol^{-1}. The interaction energies correlate well with the experimental results, and are manifested in the PES of **1e** as a narrow energy well with high barriers on both sides of the minimum, constraining the dynamics of the cyclopropyl group. Interestingly, the melting point of **1e** was 164.1 °C, which is the highest of all compounds and is 25.2 °C above that of pure **1**, supporting the occurrence of some stabilization in the cocrystal.

The ability to tame the dynamics in **1** through the introduction of a coformer, arises from a twofold effect: by reducing the rotational freedom to a single energy minimum on the PES, such as in **1a**, **1d**, and **1e**, and by increasing the energy barrier surrounding this energy minimum, such as in **1e**. In order to place these results in a wider context, a search of the CSD database[40] for cyclopropyl groups was conducted (see section VI of the ESI†). Of the 166 structures that featured both a cyclopropyl group and disorder, in 37% of the cases, the disorder involved the cyclopropyl group. With pharmaceuticals featuring increasingly complex molecules, the strategy of cocrystallization may be helpful in taming troublesome dynamics that are known to complicate crystallization, structural characterization, physicochemical stability, and commercial manufacturing.

We recognise that the amorphous phase may offer advantages over the crystalline phase in terms of solubility, but from the perspective of pharmaceutical development, an amorphous form may present significant challenges in terms of physical and chemical stability. In addition, chemical

mobility has been found to reduce chemical stability in amorphous pharmaceuticals,[21] and **1** in particular has been shown to have multiple degradation pathways.[55] As part of our investigation, we did attempt to prepare the pure amorphous form of **1**, but it quickly converted to the crystalline form within hours, precluding our investigation. Polymer-stabilized amorphous solid dispersions is a potential route to amorphous pharmaceuticals, and we note that this approach has been investigated on **1**.[56–61] However, the cost of developing and commercialising a polymer-stabilised solid dispersion can be significant, and alternative strategies to develop commercially attractive medicines are always sought, such as cocrystallisation. Interestingly, new cocrystals featuring **1** have been recently reported, and have been shown to be stable for 6 months without chemical degradation.[62]

In conclusion, we report an instance of taming dynamics in a pharmaceutical using cocrystallization as a strategy. While the pure starting material **1** has a highly dynamic cyclopropyl group and displays an additional rocking motion of the double ring backbone, X-ray crystallography, DFT calculations, and solid-state NMR results support that the cocrystals have remarkably less dynamics. The most significant changes were observed in the L-proline cocrystal, **1e**, where the cyclopropyl group is being constrained in its position by intermolecular interactions arising from the crystal packing. This study provides the first systematic evidence of the ability to tame the dynamics occurring in pharmaceuticals by cocrystallization, potentially leading towards more consistent performances and improved manufacturability.

Experimental and computational

Sample preparation

Efavirenz (**1**, >98%), 1,2-di(pyridin-4-yl)ethane (**c**, >98%), and L-proline (**e**, >99%) were purchased from Tokyo Chemical Industry. Cyclohexane-1,4-dione (**a**, 98%), 4,4′-bipyridine (**b**, 99%) and (*E*)-1,2-di(pyridin-4-yl)ethene (**d**, 97%) were purchased from Sigma Aldrich. HPLC grade acetonitrile was purchased from VWR. All cocrystals were prepared by solvent-assisted grinding for 30 minutes using a Retsch MM400 ball mill in a 5 mL stainless steel milling jar, a single 10 mm stainless steel milling ball, and a milling frequency of 30 Hz. Each cocrystal was prepared at a 300 mg scale with 30 μL of acetonitrile in either a 1 : 1 stoichiometric ratio (**1a**, **1e**) or 2 : 1 stoichiometric ratio (**1b**, **1c**, **1d**) and recovering 90% of the resulting powder.

^{13}C solid-state NMR

All samples were packed into 4 mm zirconium oxide MAS rotors, and experiments were performed on a Bruker Avance III spectrometer operating at a ^{1}H Larmor frequency of 500 MHz using a 4 mm Bruker HFX probe. A magic angle spinning rate of 11 750 Hz was used throughout all experiments. The 1D ^{13}C CPMAS spectra were acquired using a ramped contact pulse on ^{1}H (from 50% to 100% amplitude),[63] a contact time of 2 ms, a ^{1}H $\pi/2$ pulse duration of 2.5 μs, and co-adding 1024 transients. SPINAL64 proton decoupling[64] was used with a ^{1}H nutation frequency of 100 kHz and a 4.4 μs pulse length. The ^{13}C spectrum was calibrated using glycine and referenced to 176.0 ppm relative to TMS at 0 ppm.[65,66] The $T_1(^{13}$C) measurements were performed using the same cross-polarization parameters followed by an inversion recovery sequence, with a ^{13}C $\pi/2$ pulse duration of 4 μs. A total of 8 delays were used for all inversion recovery experiments, with delays adjusted to appropriately sample the T_1 curve. Temperatures were calibrated externally using the ^{207}Pb resonance of lead nitrate.[67,68] Additional ^{19}F $\rightarrow$ ^{13}C CPMAS experiments were used to measure the $T_1(^{13}$C) of the trifluoromethyl group. These experiments were performed using a 4 ms contact time with a ramped contact pulse,[63] SPINAL-64 ^{19}F decoupling at a ^{19}F nutation frequency of 62.5 kHz, and a ^{19}F $\pi/2$ pulse duration of 4 μs.

^{19}F solid-state NMR

All samples were packed into 4 mm zirconium oxide MAS rotors, and experiments were performed on a Bruker Avance III spectrometer operating at a ^{1}H Larmor frequency of 500 MHz using a 4 mm Bruker HFX probe. A magic angle spinning rate of 11 750 Hz was used throughout all experiments. The 1D ^{19}F spectra were acquired using a $\pi/2$ pulse with SPINAL64 ^{1}H decoupling at a ^{1}H nutation frequency of 100 kHz and a 4.8 μs pulse length, co-adding 32 transients. An inversion recovery sequence was used to measure the $T_1(^{19}$F) relaxation times with 8 variable delays, collecting 16 transients at each delay. These delays were manually adjusted to appropriately sample the $T_1(^{19}$F) curve of each sample. The ^{19}F chemical shifts were referenced using PTFE to −122.0 ppm.[69]

Powder X-ray diffraction

Powder X-ray diffraction experiments were performed on a Bruker D4 Endeavor diffractometer, scanning 2θ from 2° to 65° with steps of 0.02° at a rate of 5° per minute (Cu Kα$_{1/2}$ = 1.5418 Å).

Thermogravimetric analysis

Thermogravimetric analysis was performed on a TA Instrument Q2000, heating the sample in an Al pan from 25 °C to 300 °C at a constant heating rate of 10 °C min^{-1}.

NMR calculations

All DFT[70–72] calculations were performed using the gauge-including projector augmented-wave (GIPAW)[73] method as implemented in CASTEP[74] as part of Materials Studio version 17.[75] The structural model used in the calculations used the structures published on the CSD: 767883 (**1**),[37] 768815 (**1a**),[37] 767759 (**1b**),[37] 909386 (**1c**),[38] 909385 (**1d**),[38] 1847168 (**1e**).[39] The GGA PBE functional[76] was employed for all calculations,

beginning with a geometry optimization routine with constrained unit cell parameters prior to calculating the NMR chemical shifts. The geometry optimization was performed with TS DFT-D correction,[77] on the fly ultrasoft pseudopotentials, and Koelling–Harmon relativistic treatment. The cut-off energies and k-point separations can be found in Table S1 of the ESI.† NMR calculations were subsequently performed using the same parameters as the geometry optimization, apart from the cut-off energy. The calculated σ_{calc} values were extracted using a script and converted into δ_{calc} using a $\sigma_{ref}(^{13}C)$ of 170 ppm and the equation $\delta_{calc} = \sigma_{ref} - \sigma_{calc}$. The $\sigma_{iso}(^{19}F)$ were averaged between the three fluorine atoms on the same CF_3 group. The $\sigma_{ref}(^{19}F)$ values are given in the figure captions.

Transition state calculations

The transition state search calculations were performed using CASTEP, OFG ultrasoft pseudopotentials, TS DFT-D, and the linear synchronous transit method.[78,79] A k-point separation of 0.05 Å^{-1} and a cut-off energy of 700 eV was used in the calculation, optimizing the transition state. The calculations were performed on **1**, **1b**, and **1c** by specifying the disordered positions as the starting and end points, with the calculation finding the transition state between both conformations. The transition state calculation for the cyclopropyl rotation in pure **1** was performed by removing distant molecules from the unit cell in order to reduce computational costs.

Potential energy surface calculations

Potential energy surface (PES) calculations were performed using DMol3 (ref. 80 and 81) as part of Materials Studio, using the crystal structures as models and featuring periodicity. The torsion angle between the cyclopropyl group and the main efavirenz molecular fragment ($\theta_{O-C-C-C}$) was modified at steps of 10°, optimizing the structure at each step with a constraint on the torsion angles. The calculations were performed using the DNP basis set, the GGA PBE functional,[76] TS DFT-D corrections,[77] and a k-point separation of 0.05 Å^{-1}.

Crystal interactions analysis

Crystal Interaction (CrysIn), a tool developed in-house, was used to evaluate the static interactions between molecules present in a crystal based on DFT.[48] The intermolecular interaction energies in the first coordination cell of each molecule in the asymmetric unit of the crystal were calculated using B3LYP-D3/6-31G(d,p) as reported in GAUSSIAN16.[49] This is a comparable method to that employed in, for instance, the energy framework calculations in Crystal Explorer[82] or PIXEL.[83] This approach enables the quantification of the intermolecular interactions present in a crystal.[84,85]

Author contributions

PMJS conceived and designed the experiments, prepared and analyzed the samples, performed the data analysis and computational work, and prepared the manuscript. JRL, HB, LPH, SONL, and SPB designed the experiments, performed the data analysis, prepared the manuscript, supervised the work, and provided guidance.

Conflicts of interest

The authors declare no conflicts of interest.

Acknowledgements

References

1 D. J. Berry and J. W. Steed, *Adv. Drug Delivery Rev.*, 2017, **117**, 3–24.

2 G. R. Desiraju, *J. Am. Chem. Soc.*, 2013, **135**, 9952–9967.

3 P. Brázda, L. Palatinus and M. Babor, *Science*, 2019, **364**, 667–669.

4 O. Almarsson and M. J. Zaworotko, *Chem. Commun.*, 2004, 1889–1896.

5 N. K. Duggirala, M. L. Perry, O. Almarsson and M. J. Zaworotko, *Chem. Commun.*, 2016, **52**, 640–655.

6 G. Bolla and A. Nangia, *Chem. Commun.*, 2016, **52**, 8342–8360.

7 J. F. Remenar, S. L. Morissette, M. L. Peterson, B. Moulton, J. M. MacPhee, H. R. Guzmán and O. Almarsson, *J. Am. Chem. Soc.*, 2003, **125**, 8456–8457.

8 Y. Gao, J. Gao, Z. Liu, H. Kan, H. Zu, W. Sun, J. Zhang and S. Qian, *Int. J. Pharm.*, 2012, **438**, 327–335.

9 Y. Gao, H. Zu and J. Zhang, *J. Pharm. Pharmacol.*, 2011, **63**, 483–490.

10 R. Shaikh, R. Singh, G. M. Walker and D. M. Croker, *Trends Pharmacol. Sci.*, 2018, **39**, 1033–1048.

11 J. R. Lewandowski, M. E. Halse, M. Blackledge and L. Emsley, *Science*, 2015, **348**, 578–581.

12 J. A. Davey, A. M. Damry, N. K. Goto and R. A. Chica, *Nat. Chem. Biol.*, 2017, **13**, 1280–1285.

13 S. Kosol, A. Gallo, D. Griffiths, T. R. Valentic, J. Masschelein, M. Jenner, E. L. C. de Los Santos, L. Manzi, P. K. Sydor, D. Rea, S. Zhou, V. Fülöp, N. J. Oldham, S. C. Tsai, G. L. Challis and J. R. Lewandowski, *Nat. Chem.*, 2019, **11**, 913–923.

14 P. K. Biswas, S. Saha, T. Paululat and M. Schmittel, *J. Am. Chem. Soc.*, 2018, **140**, 9038–9041.

15 S. Kassem, A. T. L. Lee, D. A. Leigh, V. Marcos, L. I. Palmer and S. Pisano, *Nature*, 2017, **549**, 374–378.

16 G. De Bo, M. A. Y. Gall, S. Kuschel, J. De Winter, P. Gerbaux and D. A. Leigh, *Nat. Nanotechnol.*, 2018, **13**, 381–385.

17 J. M. Lamley, C. Öster, R. A. Stevens and J. R. Lewandowski, *Angew. Chem., Int. Ed.*, 2015, **54**, 15374–15378.

18 V. Kurauskas, S. A. Izmailov, O. N. Rogacheva, A. Hessel, I. Ayala, J. Woodhouse, A. Shilova, Y. Xue, T. Yuwen, N. Coquelle, J. P. Colletier, N. R. Skrynnikov and P. Schanda, *Nat. Commun.*, 2017, **8**, 145.

19 K. Grzybowska, M. Paluch, A. Grzybowski, Z. Wojnarowska, L. Hawelek, K. Kolodziejczyk and K. L. Ngai, *J. Phys. Chem. B*, 2010, **114**, 12792–12801.

20 E. Shalaev, K. Wu, S. Shamblin, J. F. Krzyzaniak and M. Descamps, *Adv. Drug Delivery Rev.*, 2016, **100**, 194–211.

21 S. Yoshioka and Y. Aso, *J. Pharm. Sci.*, 2007, **96**, 960–981.

22 P. M. J. Szell, S. P. Brown, L. P. Hughes, H. Blade and S. O. Nilsson Lill, *Chem. Commun.*, 2020, **56**, 14039–14042.

23 J. Baudry, *J. Am. Chem. Soc.*, 2006, **128**, 11088–11093.

24 S. Khazaei and D. Sebastiani, *J. Chem. Phys.*, 2016, **145**, 234506.

25 X. Wang, P. A. Beckmann, C. W. Mallory, A. L. Rheingold, A. G. DiPasquale, P. J. Carroll and F. B. Mallory, *J. Org. Chem.*, 2011, **76**, 5170–5176.

26 X. Wang, F. B. Mallory, C. W. Mallory, H. R. Odhner and P. A. Beckmann, *J. Chem. Phys.*, 2014, **140**, 194304.

27 P. M. J. Szell, S. Zablotny and D. L. Bryce, *Nat. Commun.*, 2019, **10**, 916.

28 H. E. Kerr, L. K. Softley, K. Suresh, A. Nangia, P. Hodgkinson and I. R. Evans, *CrystEngComm*, 2015, **17**, 6707–6715.

29 A. Pajzderska, K. Drużbicki, M. A. Gonzalez, J. Jenczyk, B. Peplińska, M. Jarek, J. Mielcarek and J. Wąsicki, *J. Phys. Chem. B*, 2014, **118**, 6670–6679.

30 D. C. Apperley, A. F. Markwell, I. Frantsuzov, A. J. Ilott, R. K. Harris and P. Hodgkinson, *Phys. Chem. Chem. Phys.*, 2013, **15**, 6422–6430.

31 X. Kong, L. A. O'Dell, V. Terskikh, E. Ye, R. Wang and G. Wu, *J. Am. Chem. Soc.*, 2012, **134**, 14609–14617.

32 R. K. Chandrappa, P. Ochsenbein, C. Martineau, M. Bonin, G. Althoff, F. Engelke, H. Malandrini, B. Castro, M. El Hajji and F. Taulelle, *Cryst. Growth Des.*, 2013, **13**, 4678–4687.

33 E. Carignani, S. Borsacchi and M. Geppi, *J. Phys. Chem. A*, 2011, **115**, 8783–8790.

34 S. O. Nilsson Lill, C. M. Widdifield, A. Pettersen, A. Svensk Ankarberg, M. Lindkvist, P. Aldred, S. Gracin, N. Shankland, K. Shankland, S. Schantz and L. Emsley, *Mol. Pharmaceutics*, 2018, **15**, 1476–1487.

35 E. Carignani, S. Borsacchi, P. Blasi, A. Schoubben and M. Geppi, *Mol. Pharmaceutics*, 2019, **16**, 2569–2578.

36 A. Pajzderska, K. Drużbicki, P. Bilski, J. Jenczyk, M. Jarek, J. Mielcarek and J. Wąsicki, *J. Phys. Chem. C*, 2019, **123**, 18364–18375.

37 S. Mahapatra, T. S. Thakur, S. Joseph, S. Varughese and G. R. Desiraju, *Cryst. Growth Des.*, 2010, **10**, 3191–3202.

38 A. C. C. de Melo, I. F. de Amorim, M. d. L. Cirqueira and F. T. Martins, *Cryst. Growth Des.*, 2013, **13**, 1558–1569.

39 M. Marques, W. Braga, J. S. Junior, L. Prado, H. Rocha, F. Ferreira, G. Ferreira and J. A. L. C. Resende, *CSD Communication*, 2019.

40 C. R. Groom, I. J. Bruno, M. P. Lightfoot and S. C. Ward, *Acta Crystallogr., Sect. B: Struct. Sci., Cryst. Eng. Mater.*, 2016, **72**, 171–179.

41 R. K. Harris, *Solid State Sci.*, 2004, **6**, 1025–1037.

42 B. Elena, G. Pintacuda, N. Mifsud and L. Emsley, *J. Am. Chem. Soc.*, 2006, **128**, 9555–9560.

43 D. A. Torchia and A. Szabo, *J. Magn. Reson.*, 1982, **49**, 107–121.

44 N. Bloembergen, E. M. Purcell and R. V. Pound, *Phys. Rev.*, 1948, **73**, 679–712.

45 L. J. Farrugia, *J. Appl. Crystallogr.*, 2012, **45**, 849–854.

46 R. Chadha, A. Saini, P. Arora, S. Chanda and Dharamvirsinghjain, *Int. J. Pharm. Pharm. Sci.*, 2012, **4**, 244–250.

47 J. B. Ngilirabanga, P. P. Rosa, M. Aucamp, Y. Kippie and H. Samsodien, *J. Drug Delivery Sci. Technol.*, 2020, **60**, 101958.

48 A. Halme, M. J. Quayle, S. O. Nilsson Lill, A. Pettersen, M. Fransson and C. Boissier, *Cryst. Growth Des.*, 2019, **19**, 3670–3680.

49 M. J. Frisch, G. W. Trucks, H. B. Schlegel, G. E. Scuseria, M. A. Robb, J. R. Cheeseman, G. Scalmani, V. Barone, G. A. Petersson, H. Nakatsuji, X. Li, M. Caricato, A. V. Marenich, J. Bloino, B. G. Janesko, R. Gomperts, B. Mennucci, H. P. Hratchian, J. V. Ortiz, A. F. Izmaylov, J. L. Sonnenberg, F. Ding Williams, F. Lipparini, F. Egidi, J. Goings, B. Peng, A. Petrone, T. Henderson, D. Ranasinghe, V. G. Zakrzewski, J. Gao, N. Rega, G. Zheng, W. Liang, M. Hada, M. Ehara, K. Toyota, R. Fukuda, J. Hasegawa, M. Ishida, T. Nakajima, Y. Honda, O. Kitao, H. Nakai, T. Vreven, K. Throssell, J. A. Montgomery Jr., J. E. Peralta, F. Ogliaro, M. J. Bearpark, J. J. Heyd, E. N. Brothers, K. N. Kudin, V. N. Staroverov, T. A. Keith, R. Kobayashi, J. Normand, K. Raghavachari, A. P. Rendell, J. C. Burant, S. S. Iyengar, J. Tomasi, M. Cossi, J. M. Millam, M. Klene, C. Adamo, R. Cammi, J. W. Ochterski, R. L. Martin, K. Morokuma, O. Farkas, J. B. Foresman and D. J. Fox, *Gaussian 16 Rev. C.01*, Wallingford, CT, 2016.

50 E. G. R. Sousa, E. M. de Carvalho, R. A. da Silva San Gil, T. C. D. Santos, L. B. Borré, O. A. Santos-Filho and J. Ellena, *J. Pharm. Sci.*, 2016, **105**, 2656–2664.

51 C. Fandaruff, G. S. Rauber, A. M. Araya-Sibaja, R. N. Pereira, C. E. M. de Campos, H. V. A. Rocha, G. A. Monti, T. Malaspina, M. A. S. Silva and S. L. Cuffini, *Cryst. Growth Des.*, 2014, **14**, 4968–4975.

52 J. R. Lewandowski, J. Sein, H. J. Sass, S. Grzesiek, M. Blackledge and L. Emsley, *J. Am. Chem. Soc.*, 2010, **132**, 8252–8254.

53 L. Catalano, S. Pérez-Estrada, G. Terraneo, T. Pilati, G. Resnati, P. Metrangolo and M. A. Garcia-Garibay, *J. Am. Chem. Soc.*, 2015, **137**, 15386–15389.

54 L. Catalano, S. Perez-Estrada, H. H. Wang, A. J.-L. Ayitou, S. I. Khan, G. Terraneo, P. Metrangolo, S. Brown and M. A. Garcia-Garibay, *J. Am. Chem. Soc.*, 2017, **139**, 843–848.

55 M. Kurmi, A. Sahu, D. K. Singh, I. P. Singh and S. Singh, *J. Pharm. Biomed. Anal.*, 2018, **148**, 170–181.

56 S. Sarabu, V. R. Kallakunta, S. Bandari, A. Batra, V. Bi, T. Durig, F. Zhang and M. A. Repka, *Carbohydr. Polym.*, 2020, **233**, 115828.

57 A. Schittny, S. Philipp-Bauer, P. Detampel, J. Huwyler and M. Puchkov, *J. Controlled Release*, 2020, **320**, 214–225.

58 H. C. Arca, L. I. Mosquera-Giraldo, D. Dahal, L. S. Taylor and K. J. Edgar, *Mol. Pharmaceutics*, 2017, **14**, 3617–3627.

59 Z. M. M. Lavra, D. Pereira de Santana and M. I. Ré, *Drug Dev. Ind. Pharm.*, 2017, **43**, 42–54.

60 J. Pawar, A. Tayade, A. Gangurde, K. Moravkar and P. Amin, *Eur. J. Pharm. Sci.*, 2016, **88**, 37–49.

61 J. Yang, K. Grey and J. Doney, *Int. J. Pharm.*, 2010, **384**, 24–31.

62 B. H. Jaswanth Gowda, S. K. Nechipadappu, S. J. Shankar, M. Chavali, K. Paul, M. G. Ahmed, A. Sanjana and H. K. Shanthala, *Mater. Today: Proc.*, 2021, DOI: 10.1016/j.matpr.2021.05.535, In press.

63 G. Metz, X. L. Wu and S. O. Smith, *J. Magn. Reson., Ser. A*, 1994, **110**, 219–227.

64 B. M. Fung, A. K. Khitrin and K. Ermolaev, *J. Magn. Reson.*, 2000, **142**, 97–101.

65 C. R. Morcombe and K. W. Zilm, *J. Magn. Reson.*, 2003, **162**, 479–486.

66 M. J. Potrzebowski, P. Tekely and Y. Dusausoy, *Solid State Nucl. Magn. Reson.*, 1998, **11**, 253–257.

67 A. Bielecki and D. P. Burum, *J. Magn. Reson.*, 1995, **116**, 215–220.

68 X. Guan and R. E. Stark, *Solid State Nucl. Magn. Reson.*, 2010, **38**, 74–76.

69 A. Vyalikh, P. Simon, E. Rosseeva, J. Buder, U. Scheler and R. Kniep, *Sci. Rep.*, 2015, **5**, 15797.

70 P. Hohenberg and W. Kohn, *Phys. Rev.*, 1964, **136**, B864.

71 W. Kohn and L. J. Sham, *Phys. Rev.*, 1965, **140**, A1133–A1138.

72 M. C. Payne, M. P. Teter, D. C. Allan, T. A. Arias and J. D. Joannopoulos, *Rev. Mod. Phys.*, 1992, **64**, 1045–1097.

73 C. J. Pickard and F. Mauri, *Phys. Rev. B: Condens. Matter Mater. Phys.*, 2001, **63**, 245101.

74 S. J. Clark, M. D. Segall, C. J. Pickard, P. J. Hasnip, M. J. Probert, K. Refson and M. C. Payne, *Z. Kristallogr.*, 2005, **220**, 567–570.

75 Dassault Systèmes BIOVIA, *Materials Studio, version 17*, Dassault Systèmes, San Diego, 2017.

76 J. P. Perdew, K. Burke and M. Ernzerhof, *Phys. Rev. Lett.*, 1996, **77**, 3865–3868.

77 A. Tkatchenko and M. Scheffler, *Phys. Rev. Lett.*, 2009, **102**, 073005.

78 N. Govind, M. Petersen, G. Fitzgerald, D. King-Smith and J. Andzelm, *Comput. Mater. Sci.*, 2003, **28**, 250–258.

79 T. A. Halgren and W. N. Lipscomb, *Chem. Phys. Lett.*, 1977, **49**, 225–232.

80 B. Delley, *J. Chem. Phys.*, 1990, **92**, 508–517.

81 B. Delley, *J. Chem. Phys.*, 2000, **113**, 7756–7764.

82 M. J. Turner, S. P. Thomas, M. W. Shi, D. Jayatilaka and M. A. Spackman, *Chem. Commun.*, 2015, **51**, 3735–3738.

83 A. Gavezzotti, *Z. Kristallogr.*, 2005, **220**, 499–510.

84 H. Abouhakim, S. O. Nilsson Lill, M. J. Quayle, S. T. Norberg, A. Hassanpour and C. M. Pask, *Acta Crystallogr., Sect. B: Struct. Sci., Cryst. Eng. Mater.*, 2020, **76**, 275–284.

85 O. D. Putra, A. Pettersen, S. O. Nilsson Lill, D. Umeda, E. Yonemochi, Y. P. Nugraha and H. Uekusa, *CrystEngComm*, 2019, **21**, 2053–2057.